Efficient Tunnel Junction Lithographic Aperture 940 nm VCSEL

Antoine Pissis, Eimantas Duda, Stefano Tirelli, Urs Siegenthaler, David Quandt, Donato Bonfrate, Pratyush Das Kanungo, Martin Spieser, and Evgeny Zibik

***Abstract*— We report on oxide free 940 nm VCSELs based on a buried tunnel junction acting as a lithographic aperture and achieving power conversion efficiency above 40%. We present the fabrication flow implementing a 2-step epitaxial growth as well as a detailed electro-optical characterization of the fabricated devices. The tunnel junction based VCSELs benefit from a uniform current distribution thanks to a low resistive n-doped top DBR. The mesa-free lithographically defined aperture enables the arrangement of compact arrays constituted of small single mode emitters. Such array configuration allows to scale up the generated optical power while maintaining a diffraction-limited Gaussian beam and limiting the impact of thermal rollover.**

***Index Terms*— 940 nm VCSEL, lithographic aperture, overgrowth, Esaki tunnel junction, diffraction-limited, thermal management.**

I. Introduction

THE concept of a vertical cavity surface emitting laser (VCSEL) was proposed by Iga in the late 1970s [1]. The first VCSEL devices suffered from low current and optical confinement resulting in poor electro-optical performance [2]. In the 1990s, the oxide aperture answered the initial lack of simultaneous electrical and optical confinement and contributed to significantly improve the performance of 850 nm and 940 nm AlGaAs VCSELs with power conversion efficiency reaching 50% [3], [4], [5]. Oxide aperture VCSELs provide today low cost and reliable solutions for datacom and sensing applications.

Yet, the oxide aperture technology has limitations. The manufacture of emitters with small diameter suffer from significant yield loss [6]. Additionally, the oxidation process requires etching a mesa structure down to the oxidation layer. The emitter pitch must be larger than the sum of the mesa trench and two times the oxidation depth. Thus, tightly packed VCSEL arrays with a pitch below 20 μm are challenging to achieve with the oxide aperture. Also, the formation of the oxide aperture introduces stress in the VCSEL mesa [7]. This stress leads to major failure mechanisms during operation. Finally, large oxide aperture VCSELs suffer from current crowding [8]. The center of their aperture is not pumped efficiently which impacts their performance.

In this work, we replace the oxide aperture with an overgrown buried tunnel junction. Buried tunnel junction demonstrated efficient lateral current confinement for 1.5 μm InP VCSEL [9], [10] and 850 nm AlGaAs VCSEL [11]. Tunnel junction is also used to stack multiple active regions in the VCSEL cavity [12], [13]. Our overgrown buried tunnel junction, located in the cavity, simultaneously confines the light and the current. The lithographic definition of the aperture enables the manufacture of VCSELs with small optical cavity [14], [15]. The absence of oxidation also eliminates the need for a mesa structure. This allows us to fabricate dense arrays of small VCSEL emitters.

This letter presents the fabrication flow of 940 nm VCSELs with tunnel junction lithographic aperture. The electrical and optical confinement of such an aperture is evaluated. Then, we discuss the modal characteristics of the fabricated devices and highlight the uniform current distribution through the emission region. Finally, we discuss the electro-optical performance and present the advantage of small emitter arrays in terms of thermal management.

II. Methods and Fabrication

The process flow of our tunnel junction based lithographic aperture VCSEL unfolds as follows. As shown in Fig. 1a, we start with the growth of the bottom structure on a n-doped substrate. The bottom structure includes a n-doped bottom AlGaAs Distributed Bragg Reflector (DBR) and a first part of the cavity containing the active region InGaAs quantum wells and ending with an Esaki tunnel junction. The Esaki tunnel junction is formed by two thin highly doped layers [16], [17]. For efficient tunneling, we use doping levels above 10^{19} cm^{-3}. To limit the introduction of optical losses related to free carrier absorption [18], the tunnel junction layers are in one of the field nodes of the longitudinal optical mode. Then, we define the emission region by lithography. We etch the tunnel junction layers and leaves a shallow protuberance which forms the emitter aperture as shown in Fig. 1b. We overgrow the patterned bottom epitaxial structure with a top structure which includes the remaining portion of the cavity and a n-doped top AlGaAs DBR as shown in Fig. 1c. The aluminum-free growth interface limits the

Manuscript received 8 December 2022; revised 2 February 2023; accepted 3 February 2023. Date of publication 28 February 2023; date of current version 3 March 2023. The work of Antoine Pissis was supported by the II-VI Laser Enterprise and the Engineering and Physical Sciences Research Council (EPRSC) Centre for Doctoral Training in Photonic Integration and Advance Data Storage (CDT PIADS), under Grant EP/L015323/1. *(Corresponding author: Antoine Pissis.)*

Antoine Pissis is with the II-VI Laser Enterprise GmbH, 8045 Zürich, Switzerland, and also with the James Watt School of Engineering, University of Glasgow, G12 8QQ Glasgow, U.K. (e-mail: antoine.pissis@coherent.com).

Eimantas Duda, Stefano Tirelli, Urs Siegenthaler, David Quandt, Donato Bonfrate, Pratyush Das Kanungo, Martin Spieser, and Evgeny Zibik are with the II-VI Laser Enterprise GmbH, 8045 Zürich, Switzerland.

Color versions of one or more figures in this letter are available at https://doi.org/10.1109/LPT.2023.3244588.

Digital Object Identifier 10.1109/LPT.2023.3244588

This work is licensed under a Creative Commons Attribution-NonCommercial-NoDerivatives 4.0 License.
For more information, see https://creativecommons.org/licenses/by-nc-nd/4.0/

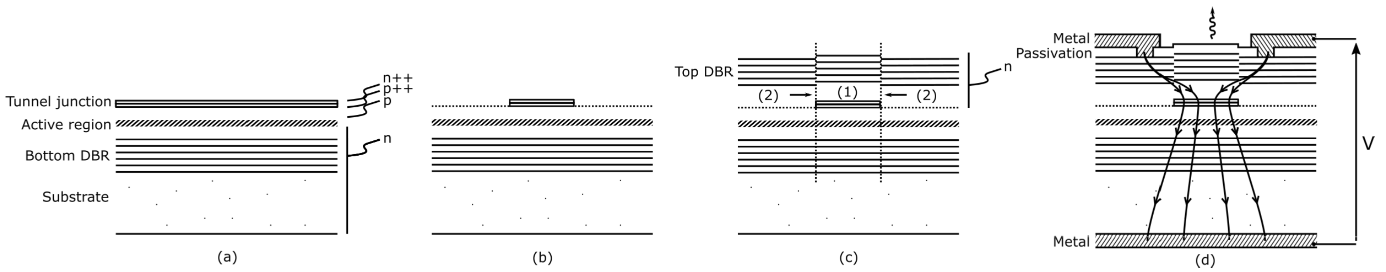

Fig. 1. Fabrication flow overview: (a) Initial growth (b) Aperture patterning (c) Top DBR overgrowth (d) Surface passivation with bottom and top metal contacts deposition. The device is operated with a positive voltage bias from bottom to top. The streamlines represent the current flow which is laterally confined towards the emission region from region (2) to region (1).

formation of oxide which prevents the generation of defects during overgrowth. Finally, the fabrication is completed with the passivation of the semiconductor surface and the deposition of metal contact as shown in Fig. 1d. Top and bottom contacts enable to drive the current through the active region.

The efficiency of the VCSEL device relies on the lateral electrical and optical confinement towards the emission region indicated by region (1) in Fig.1c.

The comparison of the voltage vs. current characteristics presented in Fig. 2a inside (region (1)) and outside (region (2)) the emission region manifests the electrical confinement. The voltage vs. current characteristics are measured, as in the normal operation of the laser, by applying a positive bias from the bottom to the top metal contacts. The characteristics follow a typical diode-like behavior for which driving a positive current requires a voltage bias above a certain turn-on voltage. Inside the emission region, with the presence of the tunnel junction, the turn-on voltage is located around 1.3 V. This turn-on voltage equals the built-in voltage of the p-n junction constituting the active region. We infer a limited contribution of the tunnel junction to the turn-on voltage. This confirms the ohmic behavior of the tunnel junction operated in reverse bias. Conversely, outside the emission region, the turn-on voltage jumps to around 10 V. The layers at the overgrowth interface have lower doping levels compared to the tunnel junction layers. When the tunnel junction is etched, the overgrowth interface turns into a reverse biased p-n junction. The 9 V increase of the turn-on voltage corresponds to the breakdown voltage of the reverse biased p-n junction. Until the operating voltage remains well below 10 V, the current flows only in the region where the tunnel junction is present i.e., the emission region. This assures efficient current confinement of the lithographic aperture.

To evaluate the optical confinement, we compare the reflectivity spectra inside and outside the emission region as reported in Fig. 2b. The reflectivity spectra are formed by the large stop band of the DBR with a narrow dip corresponding to the Fabry Perot resonance. Due to the profiling of the cavity with the etched tunnel junction layers, the optical cavity is thicker in the emission area. The resonance inside the emission region exhibits a red shift $\Delta\lambda$ compared to the outside of the emission region. According to the effective refractive index model proposed by Hadley [19], this resonance shift $\Delta\lambda$ induces an effective refractive index Δn expressed by:

$$\frac{\Delta n}{n_0} = \frac{\Delta\lambda}{\lambda_0} \tag{1}$$

where n_0 is the refractive index of the material constituting the cavity and λ_0 is the initial resonance wavelength. The measured spectra reveal a 10 nm shift between the Fabry Perot dips inside and outside the emission region, respectively 938 nm and 928 nm. According to equation 1, this is equivalent to a 1% refractive index increase towards the emission region. A similar level of refractive index shift is reported for oxide aperture VCSEL [20]. This positive refractive index shift guarantees lateral optical confinement of the emission region.

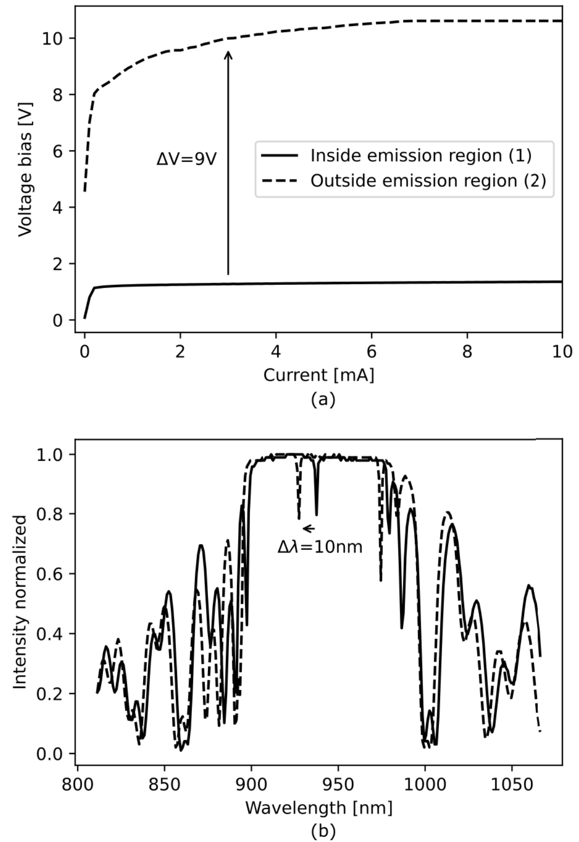

Fig. 2. Evaluation of the electrical and optical lateral confinements of the tunnel junction lithographic aperture: (a) Comparison of the voltage-current characteristics inside and outside the emission region (b) Comparison of the reflectivity spectra inside and outside the emission region.

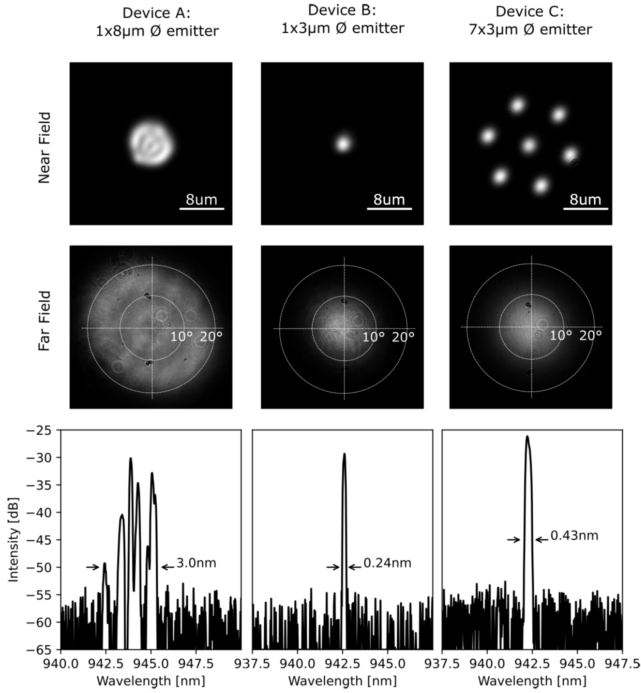

Fig. 3. Near field, far field and spectrum of devices A, B and C measured under a current density of $20\,\text{kA}\,\text{cm}^{-2}$ at 25 °C.

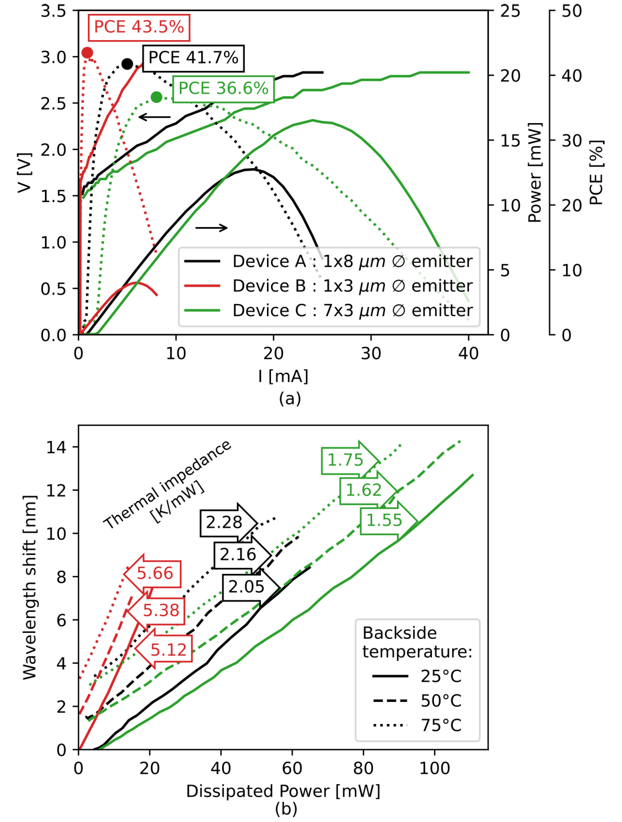

Fig. 4. Electro-optical characteristics of devices A, B and C: a) optical output power, voltage bias and power conversion efficiency vs. operating current measured at 25 °C b) emission wavelength shift vs. dissipated power where the reference wavelength is the emission wavelength at threshold under 25 °C, 50 °C and 75 °C, associated thermal impedances are annotated.

III. Results and Discussions

We fabricated tunnel junction lithographic aperture VCSEL devices with various emission area configurations. Devices A and B are respectively 8 μm and 3 μm diameter single emitters. The high resolution offered by the lithographic aperture ensures the reproducibility of emitters with 4 μm diameter and below. Device C is an array of 7 emitters with 3 μm diameter arranged on a triangular lattice. Device A and C share the same total emission area of $50\,\mu\text{m}^2$. The absence of mesa enabled a 8 μm pitch between emitters. Thanks to this compact array arrangement, device C has a similar footprint as device A.

Figure 3 presents the modal characteristics of the three devices A, B and C under an operating current density of $20\,\text{kA}\,\text{cm}^{-2}$. For all three aperture configurations, the transverse laser modes spread over the entire emission region. This reflects an uniform current distribution across the emission region. The p-doped spacer between the active region and the tunnel junction interface is significantly more resistive than the n-doped top DBR. Therefore, the lateral flow of the current in the n-doped top DBR contributes less to the total resistance path as compared to crossing the tunnel junction and the p spacer. This counteracts the current crowding and results in an uniform lateral current flow distribution.

The presence of field nodes in the near-field and the 3 nm broad spectrum with multiple high intensity peaks for the large 8 μm diameter emitter device A indicates the multimodal operation of the device. On the contrary, the small 3 μm diameter emitter of device B is small enough to support the fundamental mode only. The Gaussian near field and the 0.24 nm linewidth, limited by the resolution of the spectrometer used during the measurement, confirm the single mode operation. The multimodal operation affects the far field profile. The M^2 beam quality factor and consequently the half-angle beam divergence increase with the transverse mode order [21]. Thus, while the divergence of a single fundamental mode (order 0) beam is diffraction-limited, the divergence of a multimodal beam expands with the operating transverse mode orders. As we observed, device B exhibits a half-angle beam divergence of 10° which is twice narrower as compared to the 20° divergence angle of device A.

Replicating the small 3 μm diameter emitter of device B and forming the array of device C increases the total emission area while maintaining the single mode operation for each emitter. In the situation where these emitters are incoherent from each other, their spectrum and far field intensity profiles overlap. The array configuration of device C benefits from the diffraction-limited divergence as for the single emitter device B. As the emitters are identical, they have close emission wavelengths. The overlay of their spectrum results in a slight enlargement of the spectral linewidth to 0.43 nm.

Figure 4a presents the output optical power and voltage vs. current characteristics of devices A, B and C at 25 °C. Considering the optical power vs. current characteristics, the three devices exhibit similar slope efficiency around $0.95\,\text{mW}\,\text{mA}^{-1}$. They differ in their threshold currents with 0.85 mA, 0.20 mA and 1.8 mA for respectively devices A, B and C. In terms of threshold current density, this corresponds to $1.7\,\text{kA}\,\text{cm}^{-2}$, $2.8\,\text{kA}\,\text{cm}^{-2}$ and $3.6\,\text{kA}\,\text{cm}^{-2}$. From device B to device C, both composed of 3 μm diameter emitters, the threshold current scales with the number of emitters. Thus, devices B and C presents similar level of threshold current

density. By contrast, the large emitter device A has a two times lower threshold current density. The reduction of the emitter diameter decreases the confinement factor of the higher order modes. The reduction of the higher order modes confinement factor enables single mode operation for 3 μm diameter emitter. However, the fundamental mode's confinement factor is reduced as well which increases the threshold current density. Considering the voltage vs. current characteristics, the three devices present the same turn-on voltage at 1.5 V. These characteristics lead to a power conversion efficiency reaching 40% during the linear operation of the devices. As the devices present similar slope efficiency and voltage bias levels, the threshold current is the main factor affecting the power conversion efficiency. Thanks to its low threshold current, the single small emitter (device B) has the highest power conversion efficiency 43.5% followed by the large single emitter (device A) with 41.7% and the array (device C) with 36.6% maximum of power conversion efficiency.

The optical power of the single small emitter (device B) is below 4 mW. Thermal rollover occurs at around 5 mA and limits the maximal output optical power. One way to postpone thermal rollover is to decrease the current density by increasing the active region area. This way, the single large emitter (device A) and the array (device C) delivers more than 10 mW of optical power. Despite sharing the same total emission area and exhibiting a lower power conversion efficiency, the array reaches rollover at an operating current of 25 mA which is higher compared to the 17 mA operating current of the large single emitter. As a result, the array delivers up to 16 mW optical power which is 25% higher than the 13 mW optical power for the single large emitter. This indicates a more efficient thermal management for the array as compared to the single large emitter. The array has a larger footprint than the large single emitter. Hence, the area contributing to heat removal is larger for the array than for the large single emitter. This results in more efficient thermal removal and lower thermal impedance which allows the operation under higher current densities for the array. As reported in Fig. 4b, we measured the thermal impedance by monitoring the emission wavelength shift vs. the dissipated power corresponding to the difference of the operating electrical power and the generated optical power [22]. As expected, the single small emitter has the highest thermal impedance exceeding $5.0\,\mathrm{K\,mW^{-1}}$. The measurements confirm that heat dissipation is more efficient for the array with a thermal impedance of $1.55\,\mathrm{K\,mW^{-1}}$, 20% lower compared to $2.05\,\mathrm{K\,mW^{-1}}$ for the large single emitter at 25 °C. We also noted that the thermal impedance increases with the backside temperature while conserving the same difference between devices.

IV. Conclusion

We successfully fabricated 940 nm VCSELs with a lithographic aperture based on a thin buried Esaki tunnel junction. The tunnel junction lithographic aperture guarantees simultaneous electrical and optical confinements which enable a threshold current density as low as $2\,\mathrm{kA\,cm^{-2}}$. Unlike its oxide counterparts, the tunnel junction lithographic aperture benefits from a uniform current distribution across a mesa-free and a lithographically defined emission area. This enables easier and reproducible manufacturing of compact arrays with single mode emitters (4 μm diameter and below). Such arrays scale up the optical power while maintaining a diffraction-limited Gaussian beam and allowing efficient heat removal.

References

[1] K. Iga, "VCSEL: Born small and grown big," in *Proc. SPIE*, 2020, Art. no. 1126302.

[2] K. Tai, R. J. Fischer, K. W. Wang, S. N. G. Chu, and A. Y. Cho, "Use of implant isolation for fabrication of vertical cavity surface-emitting laser diodes," *Electron. Lett.*, vol. 25, no. 24, p. 1644, 1989.

[3] D. L. Huffaker, D. G. Deppe, K. Kumar, and T. J. Rogers, "Native-oxide defined ring contact for low threshold vertical-cavity lasers," *Appl. Phys. Lett.*, vol. 65, no. 1, pp. 97–99, Jul. 1994.

[4] K. L. Lear, K. D. Choquette, R. P. Schneider, S. P. Kilcoyne, and K. M. Geib, "Selectively oxidised vertical cavity surface emitting lasers with 50% power conversion efficiency," *Electron. Lett.*, vol. 31, no. 3, pp. 208–209, Feb. 1995.

[5] B. Weigl et al., "High-performance oxide-confined GaAs VCSELs," *IEEE J. Sel. Topics Quantum Electron.*, vol. 3, no. 2, pp. 409–415, Apr. 1997.

[6] N. Ledentsov Jr., V. Shchukin, J. Kropp, M. Agustin, and N. N. Ledentsov, "Oxide-confined leaky vertical-cavity surface-emitting lasers for single-mode operation," *SPIE Newsroom*, Aug. 2016. [Online]. Available: https://spie.org/news/6544-oxide-confined-leaky-vertical-cavity-surface-emitting-lasers-for-single-mode-operation

[7] F. Kießling et al., "Strain field of a buried oxide aperture," *Phys. Rev. B, Condens. Matter*, vol. 91, no. 7, Feb. 2015, Art. no. 075306.

[8] M. Grabherr et al., "High-power VCSELs: Single devices and densely packed 2-D-arrays," *IEEE J. Sel. Topics Quantum Electron.*, vol. 5, no. 3, pp. 495–502, 1999.

[9] M. Ortsiefer et al., "2.5-mW single-mode operation of 1.55-μm buried tunnel junction VCSELs," *IEEE Photon. Technol. Lett.*, vol. 17, no. 8, pp. 1596–1598, Jul. 25, 2005.

[10] L. Mutter, V. Iakovlev, A. Caliman, A. Mereuta, A. Sirbu, and E. Kapon, "1.3 μm-wavelength phase-locked VCSEL arrays incorporating patterned tunnel junction," *Opt. Exp.*, vol. 17, no. 10, pp. 8558–8566, 2009.

[11] P. Wong, J. Yan, T. Wu, W. Kyi, J. Pao, and M. Riaziat, "Tunnel junction 850-nm VCSEL for aperture uniformity and reliability," in *Proc. SPIE*, 2017, Art. no. 101220B.

[12] T. Knodl, A. Straub, M. Golling, R. Michalzik, and K. J. Ebeling, "Scaling behavior of bipolar cascade VCSELs," *IEEE Photon. Technol. Lett.*, vol. 13, no. 9, pp. 930–932, Sep. 2001.

[13] M. Dummer, A. Ghods, K. Tatah, and K. Johnson, "High-power single-mode multijunction VCSEL," in *Proc. 28th Int. Semiconductor Laser Conf. (ISLC)*, Oct. 2022, pp. 1–2.

[14] A. Demir, G. Zhao, S. Freisem, X. Liu, and D. G. Deppe, "Scaling properties of lithographic VCSELs," *Proc. SPIE*, vol. 7952, Feb. 2011, Art. no. 79520O.

[15] X. Yang, M. Li, G. Zhao, Y. Zhang, S. Freisem, and D. Deppe, "Small-sized lithographic single-mode VCSELs with high-power conversion efficiency," *Proc. SPIE*, vol. 9381, Mar. 2015, Art. no. 93810R.

[16] L. Esaky, "New phenomenon in narrow germanium *p–n* Junctions," *Phys. Rev. J. Arch.*, vol. 109, p. 603, Jan. 1958.

[17] P. J. Price and J. M. Radcliffe, "Esaki tunneling," *IBM J. Res. Develop.*, vol. 3, no. 4, pp. 364–371, Oct. 1959.

[18] W. J. Turner and W. E. Reese, "Absorption data of laser-type GaAs at 300° and 77°K," *J. Appl. Phys.*, vol. 35, no. 2, pp. 350–352, Feb. 1964.

[19] G. R. Hadley, "Effective index model for vertical-cavity surface-emitting lasers," *Opt. Lett.*, vol. 20, no. 13, p. 1483, 1995.

[20] R. Michazik, *Fundamentals, Technology and Applications of Vertical-Cavity Surface-Emitting Lasers*. Cham, Switzerland: Springer, 2013.

[21] A. E. Siegman, "New developments in laser resonators," *Proc. SPIE*, vol. 1224, pp. 2–14, Jun. 1990.

[22] M. Daubenschüz, "Simplified determination of the thermal resistance of vertical-cavity surface-emitting lasers," Ulm Univ. Inst. Optoelectronics, Ulm, Germany, Annu. Rep., 2015 p. 21